

# Transmission Phase Limit of Multilayer Frequency-Selective Surfaces for Transmitarray Designs

Ahmed H. Abdelrahman, *Student Member, IEEE*, Atef Z. Elsherbeni, *Fellow, IEEE*, and Fan Yang, *Senior Member, IEEE*

**Abstract**—Many transmitarray antennas are designed with multilayer frequency-selective surface (M-FSS) type elements. The goal of this paper is to reveal the transmission phase limit of M-FSS for transmitarray antenna designs. An analytical study of the transmission coefficient of multiple conductor layers separated by dielectric materials has been carried out, and the maximum transmission phase range has been determined according to the number of layers, substrate permittivity, and separation between conductor layers. It is revealed that the  $-1$ -dB transmission phase limits are  $54^\circ$ ,  $170^\circ$ ,  $308^\circ$ , and full  $360^\circ$  for single-, double-, triple-, and quad-layer FSS consisting of identical layers, respectively. Furthermore, it is shown that if  $-3$ -dB criteria is used, a triple-layer FSS is sufficient to achieve the full  $360^\circ$  phase range. The effectiveness of the analytical study has been validated through numerical simulations of several representative FSS examples.

**Index Terms**—Frequency selective surfaces (FSS), multilayer, transmission phase range, transmitarray antenna.

## I. INTRODUCTION

THE vast diversities of antennas can be classified into low gain antennas ( $<10$  dBi), middle gain antennas ( $10$  dBi– $20$  dBi), and high gain antennas ( $>20$  dBi). Transmitarray antennas belong to the high-gain antenna group. Traditionally, a high gain can be realized using two approaches: one is based on the optic theory that manipulates the geometrical curvature of antenna surface to focus the radiation beam; the other is based on antenna array theory that controls the interference of elements radiation appropriately. Representations for the first approach are the parabolic reflectors and Luneburg lens, and examples of the second approach include

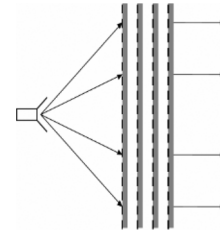


Fig. 1. Geometry of a M-FSS type transmitarray antenna.

waveguide-slot arrays and printed microstrip antenna arrays. As an emerging concept, the transmitarray antenna combines the favorable features of the optic theory and the array technique, leading to a low profile conformal design with high radiation efficiency and flexible radiation performance.

A transmitarray antenna consists of an illuminating feed source and a flat transmitting surface composed of one or multiple layers, as shown in Fig. 1. The feed source is usually located on an equivalent focal point. On the transmitting surface, there is an array of printed antenna elements. The transmission coefficients of these elements are individually designed to convert the spherical phase front from the feed to a planar phase front. As a result, a focused radiation beam can be achieved with a high gain.

There are three different techniques for transmitarray designs: multilayer frequency selective surfaces (M-FSS) [1]–[4], receiver-transmitter design [5]–[9], and metamaterial-transformation approach [10], [11]. The frequency-selective surfaces approach is popularly used to control the transmission magnitude and phase of each element in the array individually by varying the element's dimensions [1]–[4]. However, a full  $360^\circ$  phase range compensation cannot be achieved by only one layer of the printed antenna elements array [1], [2]. Thus, multilayer design in which the layers are separated by either air gap or dielectric material is required to increase the transmission phase range of the antenna element. In [3], seven conductor layers of dipole element transmitarray antenna are designed to achieve the required transmission phase range of  $360^\circ$ . A four identical layers transmitarray antenna is designed in [4], which aims to increase the transmitarray bandwidth, and achieves full transmission phase range of  $360^\circ$  using double square loop element as a unit cell. In the second approach, a transmitarray antenna is typically consisting of two planar arrays of printed antennas. One of the arrays is illuminated by the antenna feed source, and it acts as a receiver. A coupling structure or transmission lines between

Manuscript received April 11, 2013; revised August 27, 2013; accepted October 13, 2013. Date of publication November 06, 2013; date of current version January 30, 2014. This work is supported by the National Science Foundation Award # ECCS-1102269.

A. H. Abdelrahman is with the Center of Applied Electromagnetic System Research (CAESR), Electrical Engineering Department, The University of Mississippi, University, MS 38677 USA (e-mail: ahabdelr@olemiss.edu).

A. Z. Elsherbeni is with the Electrical Engineering and Computer Science Department, Colorado School of Mines, Golden, CO 80401 USA (e-mail: aelsherb@mines.edu).

F. Yang is with the Microwave and Antenna Institute, Electronic Engineering Department, Tsinghua University, Beijing 100084, China, and also with the Electrical Engineering Department, The University of Mississippi, University, MS 38677 USA (e-mail: fan\_yang@tsinghua.edu.cn).

Color versions of one or more of the figures in this paper are available online at <http://ieeexplore.ieee.org>.

Digital Object Identifier 10.1109/TAP.2013.2289313

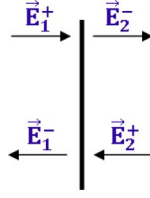


Fig. 2. Single layer with a conducting element.

both arrays are designed to achieve a specific phase and magnitude distribution over the second array, which acts as a transmitter radiating into free space [5]–[9]. Planar lens antennas with stripline delay lines are described in [5], [6]. In [7], the design and characterization of planar transmitarrays at 10 GHz with 1-bit and 2-bit phase quantization is presented. Circular polarized transmitarray are demonstrated in [8] and [9]. The third approach to control the element phase of the antenna array is to vary the effective substrate permittivity and permeability using metamaterial configuration [10], [11]. Reconfigurable and active transmitarrays for the purpose of antenna beamforming and gain improvement are discussed in [12]–[14].

This paper investigates the transmission behaviors of M-FSS for transmitarray designs. In contrast to previous publications that studied specific FSS geometries, the goal of this paper is to reveal the transmission phase limit of M-FSS structures, which will be general for arbitrary FSS geometries. It is derived that the phase limit of M-FSS is determined by the number of layers, the substrate material, and the separation between layers, and regardless of the element shape. The validity of the derived phase limits has been verified through numerical simulations of several representative FSS examples.

The paper is organized as follows. Section II derives the S-matrix of a single FSS layer and reveals its transmission phase limit. Sections III and IV study the transmission coefficients of double-layer configuration and multi-layer configurations, respectively, as a function of the spacing between layers and the substrate permittivity. The conclusion is presented in Section V.

## II. SINGLE-LAYER FSS ANALYSIS

### A. Theoretical Analysis of Single Layer FSS

A single layer with a conducting element can be considered as a two-port system [1], [2], as shown in Fig. 2. It is assumed to be illuminated on both sides. The incident and reflected plane waves are  $\vec{E}_1^+$  and  $\vec{E}_1^-$ , respectively, at the left side terminal plane. Similarly,  $\vec{E}_2^+$  and  $\vec{E}_2^-$  are the incident and reflected plane waves, respectively, at the right-side terminal plane.

According to the linear two-port networks theory [15], these four complex quantities are related to each other as

$$\begin{bmatrix} \vec{E}_1^- \\ \vec{E}_2^- \end{bmatrix} = \begin{bmatrix} S_{11} & S_{12} \\ S_{21} & S_{22} \end{bmatrix} \begin{bmatrix} \vec{E}_1^+ \\ \vec{E}_2^+ \end{bmatrix}$$

where  $[S]$  is the scattering matrix of the two-port system. Several assumptions and approximations are adopted to derive the useful features of the  $[S]$  matrix of the FSS layer.

- Assumption a): the FSS layer is symmetrical and reciprocal. Then, the following relations are satisfied [15]:

$$S_{11} = S_{22} \quad \text{and} \quad S_{12} = S_{21}. \quad (1)$$

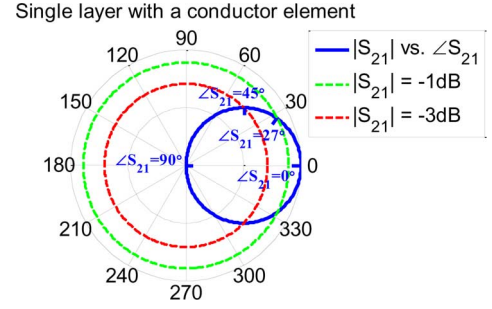


Fig. 3. Transmission coefficient of a single layer configuration.

- Assumption b): the FSS layer is lossless. Then, we have [15],

$$|S_{11}|^2 + |S_{21}|^2 = 1, \quad |S_{12}|^2 + |S_{22}|^2 = 1, \quad (2)$$

$$S_{11}S_{12}^* + S_{21}S_{22}^* = 0. \quad (3)$$

By substituting (1) in (3), we get

$$\begin{aligned} |S_{11}|e^{j(\angle S_{11})}|S_{21}|e^{-j(\angle S_{21})} \\ + |S_{21}|e^{j(\angle S_{21})}|S_{11}|e^{-j(\angle S_{11})} &= 0 \\ e^{j(\angle S_{11})}e^{-j(\angle S_{21})} + e^{j(\angle S_{21})}e^{-j(\angle S_{11})} &= 0 \\ \angle S_{11} - \angle S_{21} &= \pm \frac{\pi}{2}. \end{aligned} \quad (4)$$

Equation (4) shows an interesting observation: the phase difference between the reflected and transmitted waves of any conductor layer is  $\pi/2$  regardless of the FSS shape and transmission magnitude.

- Approximation c): the higher order harmonics of the FSS layer are relatively small and can be neglected. Then, based on the Fresnel reflection and transmission coefficients [16], we get

$$S_{21} = 1 + S_{11}. \quad (5)$$

By substituting (4) in (5), we get

$$\begin{aligned} |S_{21}|e^{j(\angle S_{21})} &= 1 + |S_{11}|e^{j(\angle S_{21} \pm \frac{\pi}{2})}, \\ |S_{21}| - |S_{11}|e^{\pm j\frac{\pi}{2}} &= e^{-j(\angle S_{21})}, \\ |S_{21}| \mp j|S_{11}| &= \cos(\angle S_{21}) - j \sin(\angle S_{21}). \end{aligned} \quad (6)$$

Equation (6) can be decomposed into two equations representing the real and imaginary parts; thus,

$$|S_{21}| = \cos(\angle S_{21}) \quad (7)$$

and

$$|S_{11}| = \pm \sin(\angle S_{21}). \quad (8)$$

It is worthwhile to explain and emphasis in (7), which reveals the relation between the transmission magnitude and phase. This relation is general and independent on the element shape. It can be demonstrated in a polar diagram as shown in Fig. 3, such that the magnitude represents  $|S_{21}|$  and the angle represents  $\angle S_{21}$ .

The transmission coefficient represents a circle on the polar diagram. The maximum transmission coefficient

TABLE I  
TRANSMISSION PHASE MAGNITUDE RELATIONSHIP  
OF A SINGLE CONDUCTOR LAYER

$ S_{21} $ (dB)	0	-1	-3
$\angle S_{21}$ (degrees)	0	$\pm 27^\circ$	$\pm 45^\circ$

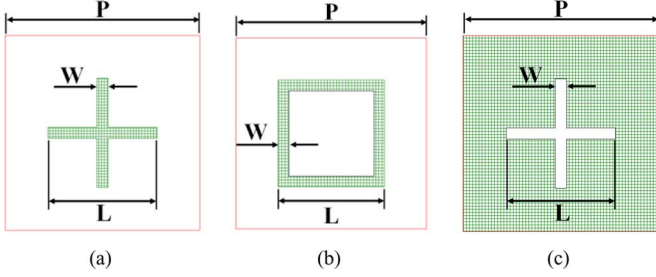


Fig. 4. Unit cells of (a) a cross dipole, (b) a square loop, and (c) a cross slot.

( $|S_{21}| = 1 = 0$  dB) is achieved only at multiples of  $2\pi$  ( $\angle S_{21} = 0^\circ, 360^\circ, \dots$ ). Practically, we may accept reduction in the transmission coefficient to a certain limit. Through this paper, we determine the transmission phase ranges for transmission magnitude limits of  $-1$  dB and  $-3$  dB. Fig. 3 shows the magnitudes of  $-1$  dB and  $-3$  dB by the dashed green and red circles, respectively. Table I presents the transmission coefficient phase at certain transmission coefficient magnitude. Accordingly, the maximum phase range that can be achieved in a single layer is  $54^\circ$  for  $-1$ -dB transmission coefficient and  $90^\circ$  for  $-3$ -dB transmission coefficient regardless of the shape of the conducting element.

Equation (8) presents the reflection magnitude as a function of the transmission phase. The positive sign is valid when  $\sin(\angle S_{21})$  is positive, and vice versa. From (1), (4), (7), and (8), the S-parameters of a single layer FSS can be represented as a function of its transmission phase [1]:

$$S_{11} = S_{22} = \sin(\angle S_{21})e^{j(\angle S_{21} \pm \frac{\pi}{2})} \quad (9)$$

$$S_{12} = S_{21} = \cos(\angle S_{21})e^{j(\angle S_{21})}. \quad (10)$$

### B. Numerical Demonstration of Single Layer FSS

To demonstrate the validity of the assumptions (a), (b), and approximation (c) as well as the accuracy of the phase limits in the previous subsection, three representative single layer unit cells of a cross dipole, a square loop, and a cross slot elements are simulated separately at 8.4 GHz.

Fig. 4 shows the three element unit cells, with half wavelength periodicity ( $P = \lambda_0/2 = 17.86$  mm), variable element length  $L$  from 7 mm to 17.5 mm, and element width ( $W = 1$  mm). The cross dipole and the square loop elements are simulated using Ansoft Designer software [17]. The cross slot element is simulated using CST Studio Suite software [18].

Fig. 5(a) and (b) is the transmission coefficient magnitude and phase, respectively, of the three elements versus the element length  $L$ . Fig. 6 depicts the transmission coefficient magnitude and phase of the three elements in polar diagrams with the variation of the element length  $L$ .

Despite the differences of the transmission coefficient results for the three elements as shown in Fig. 5, the transmission phase

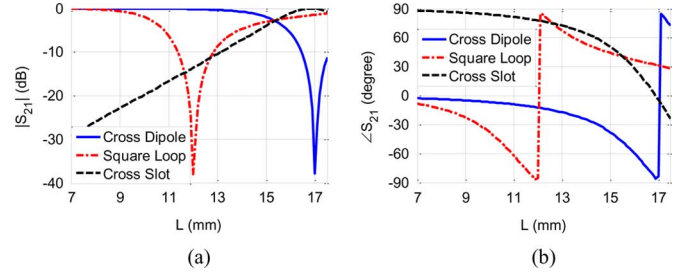


Fig. 5. Transmission coefficients of the single layer elements (a)  $|S_{21}|$  and (b)  $\angle S_{21}$ .

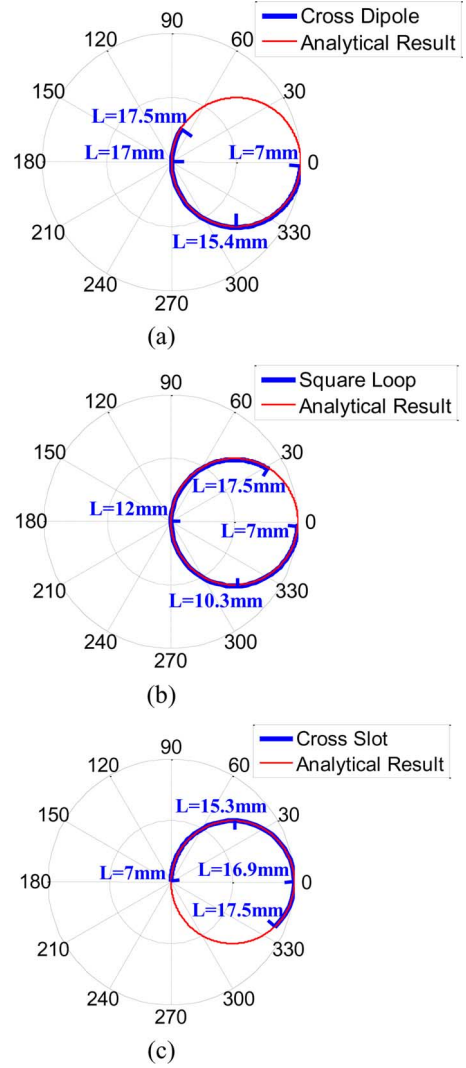


Fig. 6. Transmission coefficient presented on polar diagrams for (a) a cross dipole, (b) a square loop, and (c) a cross slot elements.

magnitude relationship of all three elements agrees with the analytical result of (7) as shown in Fig. 6. These results demonstrate the generality of the theoretical analysis, but the phase range of varying the element length  $L$  is not sufficient to cover the complete circle of Fig. 3.

It is valuable to realize the differences between the three elements according to Figs. 5 and 6. Regarding the cross dipole and the square loop elements, when the size is small ( $L = 7$  mm), the maximum transmission coefficient is achieved with a phase close to  $0^\circ$ . This represents a point located on the right edge of

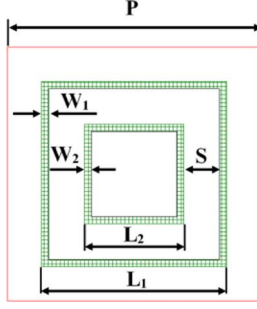


Fig. 7. Unit cell of a double square loop element [4].

the polar diagram with angle equals to  $0^\circ$  as shown in Fig. 6(a) and (b). By increasing the length  $L$ , the transmission magnitude decreases, moving clockwise on the polar diagram, until the element resonates. The resonance considers a full reflection (no transmission) and is represented by a point located at the center of the polar diagram. The cross dipole element resonates when  $L \approx \lambda_0/2$ , while the square loop element resonates when its perimeter, measured from the center of each side length, is close to one wavelength ( $L \approx \lambda_0/4 + 2W$ ). With the continued increase in the length  $L$ , the transmission coefficient starts to increase again.

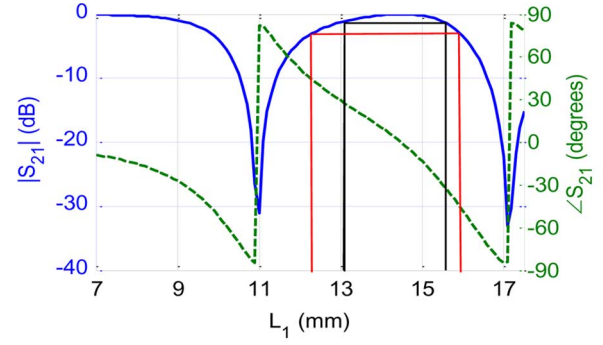
Conversely for the slot-type elements, when the length of the cross slot element is small ( $L = 7$  mm), the minimum transmission coefficient is achieved, which represent the point located at the center of the polar diagram, as shown in Fig. 6(c). By increasing the length  $L$ , the transmission magnitude increases, moving clockwise on the polar diagram, until the element resonates. The resonance for slot-type elements considers a full transmission and is represented by a point located on the right edge of the polar diagram with angle equals to  $0^\circ$ . The cross slot element resonates when  $L \approx \lambda_0/2$ . With the continued increase in the length  $L$ , the transmission coefficient starts to decrease.

### C. Single Layer of Double Square Loop Elements

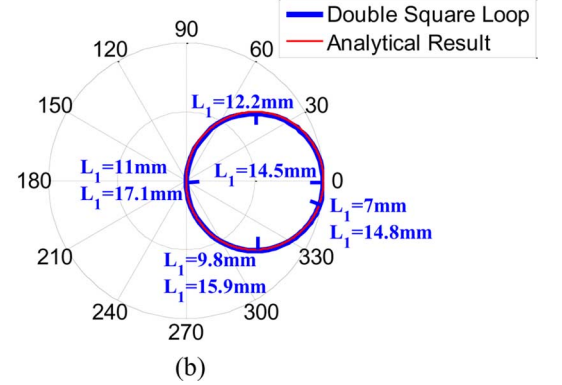
In order to achieve the maximum transmission phase range, we have to select a suitable element shape such that by varying its dimensions within the allowed periodicity of the array unit cell, the complete circle of Fig. 3 is achieved. Selecting an element with double resonance can achieve this demand, because it ensures reaching the center point on the polar diagram twice, or the point on the right edge of the polar diagram for the case of slot-type elements, by varying the element dimensions, which represents a complete circle.

An example of the double resonant elements is the double square loop shape shown in Fig. 7 [4]. A single layer unit cell of this element is simulated at 8.4 GHz with half wavelength periodicity ( $P = \lambda_0/2 = 17.86$  mm) using Ansoft Designer software [17]. The outer loop length  $L_1$  varies from  $L_1 = 7$  mm to  $L_1 = 17.5$  mm. The inner loop length  $L_2$  changes with the change of  $L_1$ , such that the separation between the two loops is constant ( $S = 2.5$  mm). The widths  $W_1$  and  $W_2$  are equal to 0.5 mm.

Fig. 8(a) presents the transmission coefficient magnitude and phase versus the outer side loop length  $L_1$ , which shows the two resonant points at  $L_1 = 11$  mm and  $L_1 = 17.1$  mm. The black solid lines contain the region that achieves transmission coef-



(a)



(b)

 Fig. 8. Transmission coefficient of the single layer double square loop element. (a)  $|S_{21}|$ , and  $\angle S_{21}$  (b) polar plot.

ficient equals to or better than  $-1$  dB, with phase ranges from  $-27^\circ$  to  $27^\circ$  (phase range of  $54^\circ$ ). Similarly, the red solid lines contain the region that achieves transmission coefficient equals to or better than  $-3$  dB, with phase ranges from  $-45^\circ$  to  $45^\circ$  (phase range of  $90^\circ$ ). These results agree with the information of Table I. Fig. 8(b) depicts the transmission coefficient magnitude and phase in a polar diagram with the variation of the outer side loop length, which conforms to the circle obtained analytically shown in Fig. 3. This design is capable of achieving the complete circle in the polar diagram.

It is worthwhile to mention that this analysis also satisfies for oblique angle of incidence. Fig. 9 depicts the transmission coefficient of the single layer double square loop element under oblique incidence angle of  $30^\circ$  for both the perpendicular and parallel polarizations. Because of oblique incidence and polarization effects, the magnitude and phase curves shift in the rectangular coordinates. However, the magnitude and phase relationship remain the same, as shown in the polar diagrams.

## III. DOUBLE LAYER FSS ANALYSIS

### A. Theoretical Analysis of Double Layer FSS

The double-layer FSS configuration shown in Fig. 10 can be considered as three cascaded sections, the first conductor layer, the dielectric substrate, and the second conductor layer. In this paper we consider both conductor layers are identical, so they have the same transmission coefficient phase  $\angle S_{21}$ . The overall transmission coefficient can be obtained through the cascading process, as illustrated in details in the Appendix.

By varying the transmission coefficient phase of the conductor layers, we can present in a polar diagram the variation of



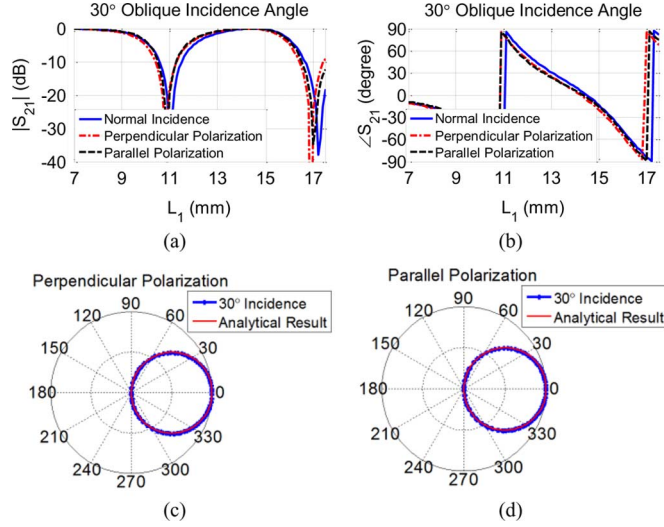


Fig. 9. Transmission coefficient of the single layer double square loop element under oblique incidence angle of  $30^\circ$ . (a)  $|S_{21}|$ , (b)  $\angle S_{21}$ , (c) perpendicular polarization in a polar diagram, and (d) parallel polarization in a polar diagram.

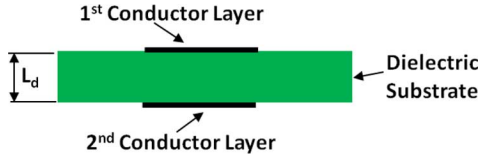


Fig. 10. Double-layer FSS configuration.

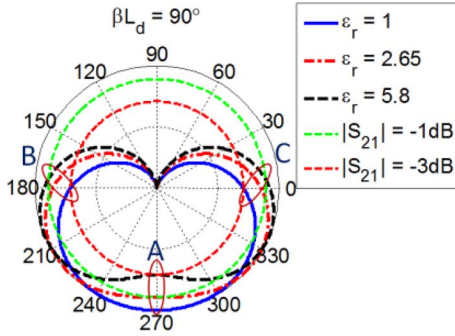


Fig. 11. Transmission coefficients of the double layer for different dielectric permittivity but constant electrical thickness of  $\beta L_d = 90^\circ$ .

the transmission coefficient magnitude and phase of the double layer configuration for different substrate permittivity as shown in Fig. 11, and for different substrate thickness as shown in Fig. 12. It is observed that the transmission phase magnitude relationships in all cases are symmetric around the vertical axis of the polar diagram.

From Fig. 11, we notice that increasing the substrate permittivity with constant electrical thickness enhances the transmission coefficient magnitude at certain phase ranges (around points B and C) but reduces it at another phase range (around point A). With the same electrical thickness of  $\beta L_d = 90^\circ$ , a substrate permittivity of  $\epsilon_r = 2.65$  has transmission coefficient reduction of  $-1$  dB at point A and the case of a substrate permittivity of  $\epsilon_r = 5.8$  has transmission coefficient reduction of  $-3$  dB at point A.

From Fig. 12, the case of substrate electrical thickness of  $\beta L_d = 90^\circ$  and permittivity of  $\epsilon_r = 1$  has no transmission coefficient reduction at point A but maximum reduction at points

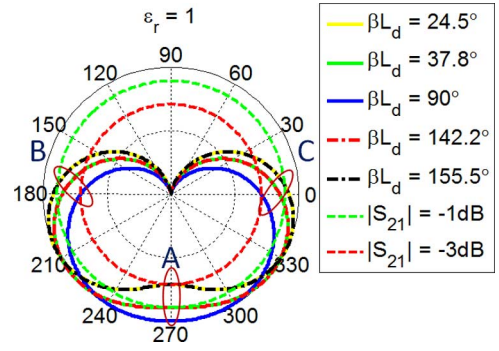


Fig. 12. Transmission coefficients of the double layer for different substrate thickness using dielectric permittivity  $\epsilon_r = 1$ .

TABLE II  
TRANSMISSION PHASE RANGE OF A DOUBLE LAYER FSS

$\epsilon_r$	$\beta L_d$	Transmission phase range (degrees)	
		$ S_{21}  \geq -1\text{dB}$	$ S_{21}  \geq -3\text{dB}$
1	$90^\circ$	$128^\circ$	$180^\circ$
	$90^\circ \pm 52.2^\circ$	$170^\circ$	$212.5^\circ$
	$90^\circ \pm 65.5^\circ$	-	$228.5^\circ$
2.65	$90^\circ$	$170^\circ$	$212.5^\circ$
5.8	$90^\circ$	-	$228.5^\circ$

B and C. Increasing or decreasing the electrical thickness away from  $\beta L_d = 90^\circ$  enhances the transmission coefficient magnitude at points B and C but reduces it at point A. The case of substrate permittivity of  $\epsilon_r = 1$ , electrical thickness of  $\beta L_d = 37.8^\circ$  and  $142.2^\circ$  ( $90^\circ \pm 52.2^\circ$ ) has transmission coefficient reduction of  $-1$  dB at point A, and the case of electrical thickness of  $\beta L_d = 24.5^\circ$  and  $155.5^\circ$  ( $90^\circ \pm 65.5^\circ$ ) has transmission coefficient reduction of  $-3$  dB at point A.

The changes of the transmission coefficient magnitude at points A, B, and C in Fig. 11 are equivalent to their changes in Fig. 12. Accordingly, we can determine the maximum transmission phase range that can be obtained from any double layer of conducting elements according to the substrate permittivity and the separation between the conductor layers regardless of the conductor element shape.

Table II summarizes the phase range for  $-1$  dB and  $-3$  dB transmission coefficient according to the substrate permittivity and electrical thickness. Accordingly, the maximum transmission phase range that can be obtained from a double layer configuration for  $-1$  dB and  $-3$  dB transmission coefficients are thus  $170^\circ$  and  $228.5^\circ$ , respectively. These phase ranges are still far from the desired phase range of  $360^\circ$  in order to support the design of transmitarrays.

### B. Numerical Demonstration of Double Layer FSS

To demonstrate the accuracy and validity of the above phase limits under the approximation of ignoring the higher order harmonics, a double layer unit cell of the double square loop element of Fig. 7 is simulated at 8.4 GHz using CST Studio Suite software [18]. In order to consider the material losses, practical materials have been selected in the numerical simulations. We used copper for conductor layers with conductivity of  $5.8 \times 10^7$  S/m. Roger and Taconic substrates were used for dielectric materials with loss tangent of 0.0009 and 0.0018, respectively.

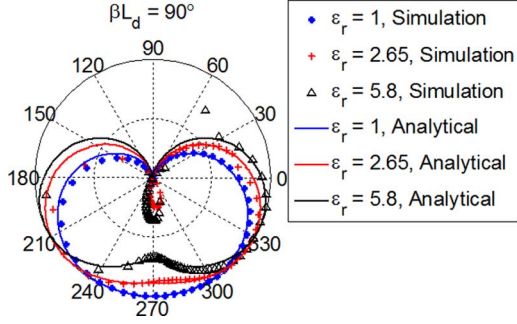


Fig. 13. Transmission coefficient presented on a polar diagram for the double square loop element in a double layer configuration.

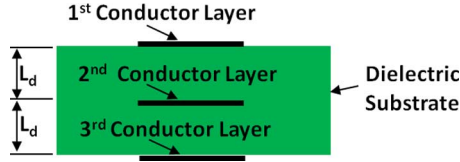


Fig. 14. Triple layer FSS configuration.

Fig. 13 depicts the transmission coefficient magnitude and phase in a polar diagram at different substrate permittivity with constant electrical thickness of  $\beta L_d = 90^\circ$ . A good agreement between full wave simulation and analytical results can be observed. Furthermore, we notice a small shift from the analytical predictions at some points when the permittivity increases. This is because the separation between layers decreases with the increase of the substrate permittivity, which hence leads to the increase of the higher order mode coupling between layers.

#### IV. MULTILAYER FSS ANALYSIS

##### A. Numerical Demonstration of Triple Layer FSS

Since the double-layer FSS cannot achieve the required transmission phase range of  $360^\circ$ , we continue to study the triple layer FSS. The S-matrix of the triple layer configuration of Fig. 14 can be obtained by cascading two more sections, the dielectric substrate and the third conductor layer, to the double layer configuration of Fig. 10. In this paper, we consider all conductor layers are identical, so they have the same transmission coefficient phase  $\angle S_{21}$ .

By varying the transmission coefficient phase of the three identical conductor layers, we present in a polar diagram the variation of the transmission coefficient of the entire triple layer configuration for different substrate permittivities and constant electrical thickness of  $\beta L_d = 90^\circ$ , as shown in Fig. 15.

From Fig. 15, we notice that at  $\beta L_d = 90^\circ$ , the transmission phase magnitude relationship in all cases are symmetric around the horizontal axis of the polar diagram. The case of  $\epsilon_r = 1$  has the smallest phase range. Increasing the substrate permittivity enhances the transmission coefficient magnitude at certain phase ranges (around points C, D and E) and reduces it at another phase ranges (around points A and B).

A substrate permittivity of  $\epsilon_r = 2$  has transmission coefficient reduction of  $-1$  dB at points A and B. Thus, we consider it the optimal permittivity that achieves maximum phase range for  $-1$  dB transmission coefficient. The case of a substrate permittivity of  $\epsilon_r = 2.5$  has its minimum transmission coefficient

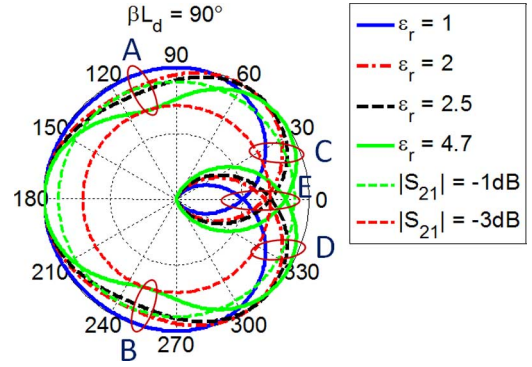

 Fig. 15. Transmission coefficient of the triple-layer FSS for different dielectric permittivity and constant electrical thickness of  $\beta L_d = 90^\circ$ .

 TABLE III  
TRANSMISSION PHASE RANGE OF A TRIPLE-LAYER FSS WITH ELECTRICAL THICKNESS BETWEEN THE CONDUCTOR LAYERS OF  $\beta L_d = 90^\circ$ 

$\epsilon_r$	Transmission phase range (degrees)	
	$ S_{21}  \geq -1\text{dB}$	$ S_{21}  \geq -3\text{dB}$
1	266°	317°
2	308°	352°
2.5	-	360°
4.7	-	360°

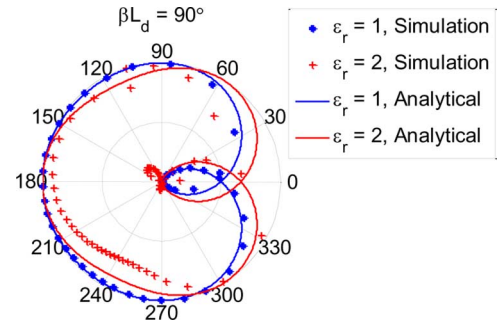


Fig. 16. Transmission coefficient presented on a polar diagram for the double square loop element in a triple layer configuration.

of  $-3$  dB at point E. Also a substrate permittivity of  $\epsilon_r = 4.7$  has its minimum transmission coefficient of  $-3$  dB at points A and B. Consequently, a full phase range of  $360^\circ$  for  $-3$ -dB transmission coefficient can be obtained using substrate permittivity between  $\epsilon_r = 2.5$  and  $\epsilon_r = 4.7$ .

Table III presents the phase range for  $-1$  dB and  $-3$  dB transmission coefficients with different substrate permittivities. In summary, the maximum transmission phase range that can be obtained using triple layer configuration is  $308^\circ$  for  $-1$ -dB transmission coefficient, and a full transmission phase range of  $360^\circ$  for  $-3$ -dB transmission coefficient.

##### B. Numerical Demonstration of Triple-Layer FSS

A triple-layer FSS consisting of the double square loop element of Fig. 7 is simulated at 8.4 GHz using CST Studio Suite software [18]. Fig. 16 presents the transmission coefficient in a polar diagram at two different substrate permittivities with constant electrical thickness of  $\beta L_d = 90^\circ$ . We notice that the numerical results conform well to the analytical results when  $\epsilon_r = 1$ . When the substrate permittivity increases, the higher order mode coupling between layers also increases, leading to a

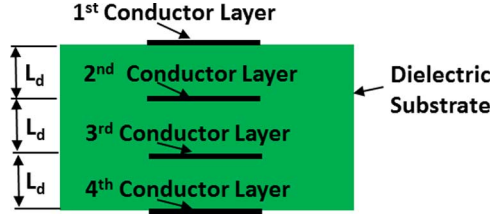


Fig. 17. Quaternary-layer FSS configuration.

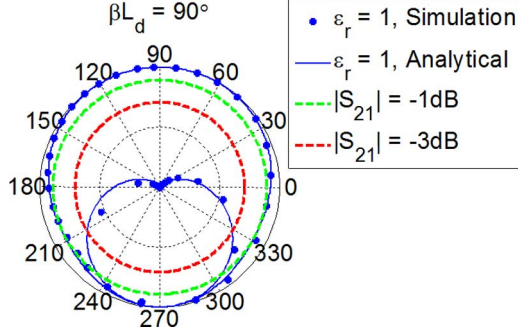


Fig. 18. Transmission coefficient presented on a polar diagram for the double square loop element in a quaternary layer configuration, with  $\epsilon_r = 1$  and  $\beta L_d = 90^\circ$ .

shift between the full wave simulations and the analytical predictions at some points. Nevertheless, the analytical results can provide a good reference for the transmission phase limits.

### C. Quaternary Layer FSS

For further improvements in the transmission phase range and to avoid the higher-order mode coupling between layers due to the high substrate permittivity, one more conductor layer can be added as shown in Fig. 17.

The polar diagram of Fig. 18 illustrates that a full transmission phase range for  $-1$ -dB transmission coefficient can be achieved using the quaternary layer of conducting elements with substrate permittivity of  $\epsilon_r = 1$  and electrical separation between layers of  $\beta L_d = 90^\circ$ . The full wave simulation results of the double square loop element of Fig. 7 in quaternary layer configuration conform to the results obtained analytically.

## V. CONCLUSION

Analytical study of the transmission coefficient of multilayer conductors separated by dielectric material is presented in this paper. The limits of the transmission phase range for  $-1$ -dB and  $-3$ -dB transmission coefficients have been derived according to the number of layers, substrate materials, and layer separations. The maximum transmission phase range of a single layer configuration for  $-1$ -dB and  $-3$ -dB transmission coefficients are  $54^\circ$  and  $90^\circ$ , respectively. The maximum transmission phase range of the double layer for  $-1$ -dB and  $-3$ -dB transmission coefficients are  $170^\circ$  and  $228.5^\circ$ , respectively. For the triple layer the maximum transmission phase of  $308^\circ$  for  $-1$ -dB transmission coefficient and a full phase range of  $360^\circ$  for  $-3$  dB transmission coefficient can be achieved. The quaternary layer can achieve full phase range of  $360^\circ$  for  $-1$ -dB transmission coefficient. These analytical limits are generally applicable, independent from the selection of a specific element shape. The pro-

posed phase range limits are validated through numerical simulations of several representative FSS geometries.

## APPENDIX

In order to obtain the S-parameters of the multilayer configurations, we should first develop the S-matrix of any two cascaded layers using the knowledge of the S-parameters of each individual layer as [1], [2]

$$S_{11}^C = \frac{S_{11}^1 S_{12}^1 S_{21}^1}{1 - S_{11}^1 S_{22}^1} + S_{11}^1 \quad (11)$$

$$S_{12}^C = S_{21}^C = \frac{S_{21}^1 S_{22}^1}{1 - S_{11}^1 S_{22}^1} \quad (12)$$

$$S_{22}^C = \frac{S_{22}^1 S_{21}^1 S_{12}^1}{1 - S_{11}^1 S_{22}^1} + S_{22}^1 \quad (13)$$

where  $S_{11}^1, S_{12}^1, S_{21}^1$ , and  $S_{22}^1$  are the S-parameters of the first layer,  $S_{11}^2, S_{12}^2, S_{21}^2$ , and  $S_{22}^2$  are the S-parameters of the second layer,  $S_{11}^C, S_{12}^C, S_{21}^C$ , and  $S_{22}^C$  are the S-parameters of cascaded two layers.

Accordingly, the S-matrix of multiple-conductor layers separated by dielectric substrate can be computed (and hence the transmission coefficient  $S_{21}$ ) by repeatedly cascading the S-parameters of the conductor layer defined in (9) and (10) and the S-parameters of the dielectric substrate defined as [19],

$$S_{11} = S_{22} = \frac{\Gamma(1 - e^{-j2\beta L_d})}{1 - \Gamma^2 e^{-j2\beta L_d}} \quad (14)$$

$$S_{12} = S_{21} = \frac{(1 - \Gamma^2)e^{-j\beta L_d}}{1 - \Gamma^2 e^{-j2\beta L_d}} \quad (15)$$

where for normal plane wave incidence

$$\Gamma = \frac{1 - \sqrt{\epsilon_r}}{1 + \sqrt{\epsilon_r}} \quad \text{and} \quad \beta = \frac{2\pi\sqrt{\epsilon_r}}{\lambda_0}.$$

It is worthwhile to notice that the S-matrix of the dielectric substrate is a function of the dielectric permittivity  $\epsilon_r$  and the substrate thickness  $L_d$ , while the S-matrix of the conducting element layer is a function of its  $\angle S_{21}$ .

For the case of oblique incidence, both  $\Gamma$  and  $\beta$  have to be updated based on the analysis of the reflections and transmissions at oblique wave incidence as discussed in [19].

## REFERENCES

- [1] S. Datthanasombat, "Analysis and Design of High-Gain Space-Fed Passive Microstrip Array Antennas," Doctoral dissertation, Univ. of Southern California, Los Angeles, CA, USA, 2003.
- [2] S. Datthanasombat, A. Prata, Jr., L. R. Amaro, J. A. Harrell, S. Spitz, and J. Perret, "Layered lens antenna," in *Proc. IEEE Antennas Propag. Soc. Int. Symp.*, Boston, MA, USA, 2001, pp. 777–780.
- [3] R. Milne, "Dipole array lens antenna," *IEEE Trans. Antennas Propag.*, vol. AP-30, no. 4, pp. 704–712, Jul. 1982.
- [4] C. G. M. Ryan, M. Reza, J. Shaker, J. R. Bray, Y. M. M. Antar, and A. Ittipiboon, "A wideband transmitarray using dual-resonant double square rings," *IEEE Trans. Antenna Propag.*, vol. 58, no. 5, pp. 1486–1493, May 2010.
- [5] D. M. Pozar, "Flat lens antenna concept using aperture coupled microstrip patches," *Electron. Lett.*, vol. 32, no. 23, pp. 2109–2111, Nov. 1996.
- [6] P. Padilla de la Torre and M. Sierra-Castaner, "Design and prototype of a 12-GHz transmit-array," *Microw. Opt. Technol. Lett.*, vol. 49, no. 12, pp. 3020–3026, Dec. 2007.

- [7] H. Kaouach, L. Dussopt, R. Sauleau, and T. Koleck, "Design and demonstration of an X-band transmit-array," in *Proc. 4th Eur. Conf. Antennas Propag. (EuCAP)*, 2010, pp. 1–5.
- [8] H. Kaouach, L. Dussopt, R. Sauleau, and T. Koleck, "X-band transmit-arrays with linear and circular polarization," in *3rd Eur. Conf. Antennas Propag. (EuCAP)*, 2009, pp. 1191–1195.
- [9] R. Phillion and M. Okoniewski, "Analysis of a transmit-array antenna for circular polarization," in *Proc. 26th Annu. Rev. Progress Appl. Comput. Electromagn. (ACES)*, Tampere, Finland, 2010, pp. 804–807.
- [10] S. Kamada, N. Michishita, and Y. Yamada, "Metamaterial lens antenna using dielectric resonators for wide angle beam scanning," in *Proc. IEEE Antennas Propag. Soc. Int. Symp. (APS-URSI)*, 2010, pp. 1–4.
- [11] Q. Cheng, H. F. Ma, and T. J. Cui, "Broadband planar Luneburg lens based on complementary metamaterials," *Appl. Phys. Lett.*, vol. 95, no. 18, pp. 181901-1–181901-3, Nov. 2009.
- [12] H. J. Song and M. E. Bialkowski, "Transmit array of transistor amplifiers illuminated by a patch array in the reactive near-field region," *IEEE Trans. Microw. Theory Tech.*, vol. 49, no. 3, pp. 470–475, Mar. 2001.
- [13] C.-C. Cheng, B. Lakshminarayanan, and A. A.- Tamijani, "Programmable lens-array antenna with monolithically integrated MEMS switches," *IEEE Trans. Microw. Theory Techn.*, vol. 57, no. 8, pp. 1874–1884, Aug. 2009.
- [14] P. Padilla, A. M. Acevedo, M. S.- Castañer, and M. S. Pérez, "Electronically reconfigurable transmitarray at Ku band for microwave applications," *IEEE Trans. Antennas Propag.*, vol. 58, no. 8, pp. 2571–2579, Aug. 2010.
- [15] D. M. Pozar, *Microwave Engineering*, 3rd ed. New York, NY, USA: Wiley, 2005.
- [16] B. A. Munk, *Frequency Selective Surfaces, Theory and Design*. New York, NY, USA: Wiley, 2000.
- [17] Ansoft Corporation, Ansoft Designer. Pittsburgh, PA, USA, 2010, version 6.1.0.
- [18] CST Microwave Studio, Feb. 24, 2012, version 2012.01.
- [19] C. A. Balanis, *Adv. Eng. Electromagn.*, 2nd ed. New York, NY, USA: Wiley, 2012.



**Ahmed H. Abdelrahman** (S'13) received the B.S. and M.S. degrees in electrical engineering, electronics, and communications from Ain Shams University, Cairo, Egypt, in 2001 and 2010, respectively. He is currently working toward the Ph.D. degree in electrical engineering at the University of Mississippi, University, MS, USA.

Since 2011, he has been a Research Assistant at The Center for Applied Electromagnetic Systems Research (CAESR), Electrical Engineering Department at The University of Mississippi. His research inter-

ests include antenna theory, designs, and measurements, antenna feed networks, and reflectarray and transmitarray antenna designs. He worked as an RF engineer and communication system engineer in building the low earth orbit satellite Egyptsat-1.

Mr. Abdelrahman has received the third place, student paper competition award at the 2013 ACES annual conference. He possess over eight years of experience in satellite communications industry.



**Fan Yang** (S'96–M'03–SM'08) received the B.S. and M.S. degrees from Tsinghua University, Beijing, China, in 1997 and 1999, respectively, and the Ph.D. degree from the University of California at Los Angeles (UCLA), in 2002.

From 1994 to 1999, he was a Research Assistant with the State Key Laboratory of Microwave and Digital Communications, Tsinghua University. From 1999 to 2004, he was a Graduate Student Researcher with the Antenna Laboratory, UCLA. From 2002 to 2004, he was a Post-Doctoral Research Engineer and

Instructor with the Electrical Engineering Department, UCLA. In August 2004, he joined the Electrical Engineering Department, The University of Mississippi, as an Assistant Professor, and was promoted to an Associate Professor. In 2010, he became a Professor with the Electronic Engineering Department, Tsinghua University, and has served as the Director of the Microwave and Antenna Institute since then. His research interests include antenna theory, designs, and measurements, electromagnetic band gap (EBG) structures and their applications, computational electromagnetics and optimization techniques, and applied electromagnetic systems. He has published over 200 journal articles and conference papers, five book chapters, and three books entitled *Scattering Analysis of Periodic Structures Using Finite-Difference Time-Domain Method* (Morgan & Claypool, 2012), *Electromagnetic Band Gap Structures in Antenna Engineering* (Cambridge Univ. Press, 2009), and *Electromagnetics and Antenna Optimization Using Taguchi's Method* (Morgan & Claypool, 2007).

Dr. Yang serves as an Associate Editor for the IEEE TRANSACTIONS ON ANTENNAS AND PROPAGATION and *Applied Computational Electromagnetics Society (ACES) Journal*. He is also a frequent reviewer for over 20 scientific journals and book publishers. He has chaired numerous technical sessions in various international symposia. He has been the recipient of several prestigious awards and recognitions, including the 2004 Certificate for Exceptional Accomplishment in Research and Professional Development Award of UCLA, the Young Scientist Award of the 2005 URSI General Assembly and of the 2007 International Symposium on Electromagnetic Theory, the 2008 Junior Faculty Research Award of the University of Mississippi, the 2009 inaugural IEEE Donald G. Dudley Jr. Undergraduate Teaching Award, and the 2011 Recipient of Global Experts Program of China.



**Atef Z. Elsherbeni** (S'84–M'86–SM'91–F'07) received the Ph.D. degree in electrical engineering from Manitoba University, Winnipeg, MB, Canada, in 1987.

He joined the University of Mississippi, University, MS, USA, in August 1987 as an Assistant Professor of Electrical Engineering. He advanced to the Associate Professor rank on July 1991, and to the Professor rank on July 1997. At the University of Mississippi, he was also the Director of the School of Engineering CAD Lab from August 2002 to Au-

gust 2013, the Director of the Center for Applied Electromagnetic Systems Research (CAESR) from July 2011 to August 2013, and the Associate Dean of Engineering for Research and Graduate Programs from 2009 to 2013. He was appointed as Adjunct Professor at the Department of Electrical Engineering and Computer Science, L.C. Smith College of Engineering and Computer Science, Syracuse University, in January 2004. He spent a sabbatical term in 1996 at the Electrical Engineering Department, University of California at Los Angeles (UCLA) and was a Visiting Professor at Magdeburg University in Germany during the summer of 2005 and at Tampere University of Technology in Finland during the summer of 2007. He was a Finland Distinguished Professor from 2009 to 2011.

Dr. Elsherbeni became the Dobelman Distinguished Chair and Professor of Electrical Engineering and Computer Science at Colorado School of Mines in August 2013. He is a fellow of the Applied Computational Electromagnetic Society (ACES) and the Editor-in-Chief for *ACES Journal*.